Advanced resistivity model for arbitrary magnetization orientation applied to a series of compressive- to tensile-strained (Ga,Mn)As layers

W. Limmer,* J. Daeubler, L. Dreher, M. Glunk, W. Schoch, S. Schwaiger, and R. Sauer
Institut für Halbleiterphysik, Universität Ulm, 89069 Ulm, Germany

(Received 18 February 2008; revised manuscript received 1 May 2008; published 30 May 2008)

The longitudinal and transverse resistivities of differently strained (Ga,Mn)As layers are theoretically and experimentally studied as a function of the magnetization orientation. The strain in the series of (Ga,Mn)As layers is gradually varied from compressive to tensile using (In,Ga)As templates with different In concentrations. Analytical expressions for the resistivities are derived from a series expansion of the resistivity tensor with respect to the direction cosines of the magnetization. In order to quantitatively model the experimental data, terms up to the fourth order have to be included. The expressions derived are generally valid for any single-crystalline cubic and tetragonal ferromagnet and apply to arbitrary surface orientations and current directions. The model phenomenologically incorporates the longitudinal and transverse anisotropic magnetoresistance as well as the anomalous Hall effect. The resistivity parameters obtained from a comparison between experiment and theory are found to systematically vary with the strain in the layer.

DOI: 10.1103/PhysRevB.77.205210 PACS number(s): 75.50.Pp, 75.47.−m, 75.30.Gw

I. INTRODUCTION

The implementation of ferromagnetism in III-V semiconductors by incorporating high concentrations of magnetic elements into the group-III sublattice has opened the prospect of extending conventional semiconductor technology to magnetic applications.[1–3] A prominent example, which is presently intensely studied, is the diluted ferromagnetic semiconductor (Ga,Mn)As. Even though the Curie temperatures reported so far are well below room temperature, it represents a potential candidate or at least an ideal test system for spintronic applications due to its compatibility with the standard semiconductor GaAs. During the past decade, considerable progress has been made in understanding the basic structural, electronic, and magnetic properties of (Ga,Mn)As.[3] Longitudinal anisotropic magnetoresistance[4–8] (AMR) and transverse AMR, often called as planar Hall effect,[9] anomalous Hall effect (AHE),[10–12] and magnetic anisotropy (MA),[13,14] have been established as characteristic features, making (Ga,Mn)As potentially suitable for field-sensitive devices and nonvolatile memories.[15–17] Great effort has been made to understand the microscopic mechanisms behind the observed magnetic phenomena and to obtain, theoretically and experimentally, values for the corresponding physical parameters. In particular, the storage and processing of information by manipulating the magnetization as well as the readout via electrical signals demand a precise knowledge of the parameters controlling the MA and the AMR. It has been shown that both the MA and the AMR are affected by temperature, hole density, and strain.[1,18–23] For example, changing the strain from compressive to tensile, the surface normal which usually represents a magnetic hard axis in compressively strained (Ga,Mn)As layers turns into an easy axis in tensily strained layers.[1,19,24]

As demonstrated in Ref. 25, angle-dependent magnetotransport measurements, performed at different strengths of an external magnetic field, are a genuine alternative to ferromagnetic resonance spectroscopy[19,26] for probing the MA in (Ga,Mn)As. The application of this method, however, requires analytical expressions for the longitudinal and transverse resistivities ρ_{long} and ρ_{trans}, respectively, correctly describing the AMR and the AHE. Based on symmetry considerations, such expressions can be derived in a phenomenological way by writing the resistivity tensor as a series expansion with respect to the direction cosines of the magnetization. In Ref. 25, the angle-dependent magnetotransport data of compressively strained (Ga,Mn)As layers, grown on (001)- and (113)A-oriented GaAs substrates, could be well simulated considering only terms up to the second order.

In the present work, we systematically study the influence of vertical strain on the AMR and the AHE, investigating a series of compressive- to tensile-strained (Ga,Mn)As layers, grown on (In,Ga)As templates with different In contents. An advanced macroscopic model is presented that phenomenologically describes the dependence of ρ_{long} and ρ_{trans} on the magnetization orientation for cubic ferromagnets with tetragonal distortion along [001]. The analytical expressions for ρ_{long} and ρ_{trans} are first discussed for a variety of configurations with in-plane and out-of-plane magnetizations and are then used to analyze the angle-dependent resistivities recorded from the (Ga,Mn)As layers under study. In contrast to Ref. 25, distinct features in the longitudinal out-of-plane AMR occurred which can only be described by taking into account terms up to the fourth order in the magnetization components. Finally, the resistivity parameters, determined by fitting the calculated curves to the experimental data, are discussed as a function of the vertical strain in the layer. The model presented in this work applies not only to (Ga,Mn)As but also most generally to single-crystalline cubic and tetragonal ferromagnets.

II. EXPERIMENTAL DETAILS

A series of differently strained (Ga,Mn)As layers with constant thickness of ~180 nm and Mn concentration of ~5% was grown by low-temperature molecular-beam epitaxy on (In,Ga)As templates in the following way: After ther-

mal deoxidation, a 30 nm thick GaAs buffer layer was grown at a substrate temperature of $T_S \approx 580$ °C on semi-insulating GaAs(001). Then, the growth was interrupted, T_S was lowered to ~430 °C, and a graded (In,Ga)As layer with a thickness between 0 and 5 μm was deposited following the method described in Ref. 27. In order to minimize the number of threading dislocations and to end up with different lateral lattice constants in the (In,Ga)As templates, the In content was continuously increased in each template from 2% up to a maximum value of 13%. Prior to the epitaxy of (Ga,Mn)As, the growth was again interrupted and T_S was lowered to ~250 °C. High-resolution x-ray diffraction reciprocal space mapping (RSM) of the (224) reflex was used to determine the vertical strain $\varepsilon_{zz}=(a_\perp - a_{\mathrm{rel}})/a_{\mathrm{rel}}$ of the (Ga,Mn)As layers, where the relaxed lattice constants a_{rel} were derived from the lateral and vertical lattice constants $a_\parallel$ and $a_\perp$, respectively, applying Hooke's law. The values of ε_{zz} were found to gradually vary from +0.24% for the compressive-strained sample without (In,Ga)As template to −0.46% for the tensile-strained sample with 13% In. Moreover, RSM showed that the (In,Ga)As layers were almost completely relaxed whereas the (Ga,Mn)As layers were fully strained. Further details of the growth procedure and the RSM method will be presented elsewhere.

For the magnetotransport studies two types of Hall bars with current directions along [100] and [110] were prepared on several pieces of the cleaved samples. The width of the Hall bars is 0.3 mm and the longitudinal voltage probes are separated by 1 mm. High-field magnetotransport measurements (up to 14.5 T) at 4.2 K yielded hole densities for the as-grown samples between 3×10^{20} and 4×10^{20} cm^{-3}. Least-squares fits were performed to separate the contributions of the ordinary and anomalous Hall effect. Curie temperatures between 61 and 83 K were estimated from the peak positions of the temperature-dependent sheet resistivities at 10 mT. For the angle-dependent magnetotransport measurements, carried out at 4.2 K, the Hall bars were mounted on the sample holder of a liquid-He-bath cryostat, which was positioned between the poles of an electromagnet system providing a maximum field strength of 0.68 T. The sample holder has two perpendicular axes of rotation, allowing for any orientation of the Hall bars with respect to the applied magnetic field $\boldsymbol{H}$.

III. THEORETICAL MODEL

The macroscopic theoretical model presented in this paper is based on the assumption that the sample area probed by magnetotransport can be approximately treated as a single homogeneous ferromagnetic domain. It provides analytical expressions for the electrical resistivities as a function of the magnetization orientation. Although the single-domain picture is known to usually break down in situations where the magnetic system is undergoing a magnetization reversal process, it has been successfully applied to the description of a variety of magnetization-related phenomena in (Ga,Mn)As, particularly at sufficiently high external magnetic fields.

Given a single ferromagnetic domain, the macroscopic magnetization is described by the vector $\boldsymbol{M}=M\boldsymbol{m}$, where M denotes its magnitude and the unit vector $\boldsymbol{m}$ with the components m_x, m_y, and m_z its orientation. Throughout this paper, all vector components labeled by x, y, and z refer to the cubic or tetragonal coordinate system associated with the [100], [010], and [001] crystal directions, respectively.

A. Longitudinal and transverse resistivities

We consider a standard configuration for magnetotransport measurements where the longitudinal voltage is probed along and the transverse voltage across the direction $\boldsymbol{j}$ of a homogeneous current with density $\boldsymbol{J}=J\boldsymbol{j}$. Accordingly, we introduce a right-handed coordinate system with unit vectors $\boldsymbol{j}$, $\boldsymbol{t}$, and $\boldsymbol{n}=\boldsymbol{j}\times\boldsymbol{t}$ so that $\boldsymbol{t}$ defines the transverse direction and $\boldsymbol{n}$ typically the surface normal. The measured voltages arise from the components $E_{\mathrm{long}}=\boldsymbol{j}\cdot\boldsymbol{E}$ and $E_{\mathrm{trans}}=\boldsymbol{t}\cdot\boldsymbol{E}$ of the electric field $\boldsymbol{E}$. Starting from Ohm's law $\boldsymbol{E}=\bar{\rho}\cdot\boldsymbol{J}$ with the resistivity tensor $\bar{\rho}$, the longitudinal resistivity ρ_{long} (sheet resistivity) and transverse resistivity ρ_{trans} (Hall resistivity) can be written as

$$\rho_{\mathrm{long}} = \frac{E_{\mathrm{long}}}{J} = \boldsymbol{j}\cdot\bar{\rho}\cdot\boldsymbol{j}, \quad \rho_{\mathrm{trans}} = \frac{E_{\mathrm{trans}}}{J} = \boldsymbol{t}\cdot\bar{\rho}\cdot\boldsymbol{j}. \tag{1}$$

1. Resistivity tensor

Following the ansatz of Birss,[28] we derive the dependence of ρ_{long} and ρ_{trans} on the magnetization orientation $\boldsymbol{m}$ in a phenomenological approach by writing the components ρ_{ij} of the resistivity tensor $\bar{\rho}$ as series expansions with respect to m_x, m_y, and m_z. In Ref. 25, we have presented analytical expressions for ρ_{long} and ρ_{trans} including the terms up to the second order. Now, forced by the experimental results, we substantially extend this model by taking into account the terms up to the fourth order. Using the Einstein summation convention, the series expansions read as

$$\rho_{ij} = a_{ij} + a_{kij}m_k + a_{klij}m_k m_l + a_{klmij}m_k m_l m_m + \cdots, \tag{2}$$

where the components of the galvanomagnetic tensors $a_{ij}, a_{kij}, \ldots$ appear as expansion coefficients. For crystals with cubic symmetry T_d and tetragonal symmetry D_{2d}, most of the expansion coefficients are equal in pairs or vanish. The use of generating symmetry matrices to obtain the relationship between the coefficients is described in Appendix A. The resulting resistivity tensor for tetragonal symmetry can be separated into two terms,

$$\bar{\rho}_{\mathrm{tetragonal}} = \bar{\rho}_{\mathrm{cubic}} + \Delta\bar{\rho}, \tag{3}$$

where $\bar{\rho}_{\mathrm{cubic}}$ is the resistivity tensor for cubic symmetry and $\Delta\bar{\rho}$ a difference term that vanishes in the case of perfect cubic symmetry. Writing $\bar{\rho}_{\mathrm{tetragonal}}$ in ascending powers of m_x, m_y, and m_z, our calculations yield the expressions

$$\bar{\rho}_{\mathrm{cubic}} = A\begin{pmatrix} 1 & 0 & 0 \\ 0 & 1 & 0 \\ 0 & 0 & 1 \end{pmatrix} + B\begin{pmatrix} 0 & m_z & -m_y \\ -m_z & 0 & m_x \\ m_y & -m_x & 0 \end{pmatrix} + C_1\begin{pmatrix} m_x^2 & 0 & 0 \\ 0 & m_y^2 & 0 \\ 0 & 0 & m_z^2 \end{pmatrix} + C_2\begin{pmatrix} 0 & m_x m_y & m_x m_z \\ m_x m_y & 0 & m_y m_z \\ m_x m_z & m_y m_z & 0 \end{pmatrix} + D\begin{pmatrix} 0 & m_z^3 & -m_y^3 \\ -m_z^3 & 0 & m_x^3 \\ m_y^3 & -m_x^3 & 0 \end{pmatrix}$$
$$+ E_1\begin{pmatrix} m_x^4 & 0 & 0 \\ 0 & m_y^4 & 0 \\ 0 & 0 & m_z^4 \end{pmatrix} + E_2\begin{pmatrix} m_y^2 m_z^2 & 0 & 0 \\ 0 & m_x^2 m_z^2 & 0 \\ 0 & 0 & m_x^2 m_y^2 \end{pmatrix} + E_3\begin{pmatrix} 0 & m_x m_y m_z^2 & m_x m_y^2 m_z \\ m_x m_y m_z^2 & 0 & m_x^2 m_y m_z \\ m_x m_y^2 m_z & m_x^2 m_y m_z & 0 \end{pmatrix}, \tag{4}$$

$$\Delta\bar{\rho} = \begin{pmatrix} 0 & 0 & 0 \\ 0 & 0 & 0 \\ 0 & 0 & a \end{pmatrix} + \begin{pmatrix} 0 & b m_z & 0 \\ -b m_z & 0 & 0 \\ 0 & 0 & 0 \end{pmatrix} + \begin{pmatrix} c_3 m_z^2 & 0 & c_2 m_x m_z \\ 0 & c_3 m_z^2 & c_2 m_y m_z \\ c_2 m_x m_z & c_2 m_y m_z & c_1 m_z^2 \end{pmatrix} + \begin{pmatrix} 0 & d_1 m_z^3 & -d_2 m_y m_z^2 \\ -d_1 m_z^3 & 0 & d_2 m_x m_z^2 \\ d_2 m_y m_z^2 & -d_2 m_x m_z^2 & 0 \end{pmatrix}$$
$$+ \begin{pmatrix} e_2 m_y^2 m_z^2 + e_4 m_z^4 & e_3 m_x m_y m_z^2 & e_6 m_x m_y^2 m_z + e_7 m_x m_z^3 \\ e_3 m_x m_y m_z^2 & e_2 m_x^2 m_z^2 + e_4 m_z^4 & e_6 m_x^2 m_y m_z + e_7 m_y m_z^3 \\ e_6 m_x m_y^2 m_z + e_7 m_x m_z^3 & e_6 m_x^2 m_y m_z + e_7 m_y m_z^3 & e_5 m_x^2 m_y^2 + e_1 m_z^4 \end{pmatrix}. \tag{5}$$

Deriving the above equations, we repeatedly made use of the trivial identity

$$|\boldsymbol{m}|^2 = m_x^2 + m_y^2 + m_z^2 = 1. \tag{6}$$

The expansion parameters $A, \ldots, E_3$ and $a, \ldots, e_7$ are linear combinations of the nonvanishing expansion coefficients as specified in Eqs. (A3) and (A4), respectively. It should be noted that the present notation is partially different from that used in Ref. 25.

For cubic ferromagnets with a small tetragonal distortion along [001], as in the case of the (Ga,Mn)As layers under investigation, the expansion parameters are expected to linearly vary with ε_{zz}. The parameters A and a, just as all other expansion parameters, then read as

$$A = A_{\mathrm{rel}} + \varepsilon_{zz} A', \quad a = \varepsilon_{zz} a'. \tag{7}$$

While a vanishes for zero strain, A becomes identical to A_{rel}, describing the resistivity of the relaxed cubic crystal.

Once the resistivity tensor $\bar{\rho}$ is known, analytical expressions for the dependence of ρ_{long} and ρ_{trans} on the magnetization orientation can be derived using Eqs. (1). The detailed representation of $\bar{\rho}$ in Eqs. (4) and (5) allows us to examine the resistivities for any current direction $\boldsymbol{j}$ and any orientation $\boldsymbol{t}$ of the transverse voltage probe relative to the crystal axes, provided that the crystal exhibits cubic or tetragonal symmetry. For a concise presentation of the results, it is convenient to replace the components m_x, m_y, and m_z of $\boldsymbol{m}$ referring to the cubic or tetragonal crystal axes with m_j, m_t, and m_n referring to the more experiment-related coordinate system defined by $\boldsymbol{j}$, $\boldsymbol{t}$, and $\boldsymbol{n}$ according to

$$m_i = j_i m_j + t_i m_t + n_i m_n \quad (i = x, y, z). \tag{8}$$

Consequently, Eq. (6) has to be rewritten as

$$|\boldsymbol{m}|^2 = m_j^2 + m_t^2 + m_n^2 = 1. \tag{9}$$

For the rest of the paper, we exclusively focus on the most common case of a current flow parallel to the surface of a (001)-oriented sample and examine in detail the two situations where the current direction is along [100] and [110].

2. ρ_{long} and ρ_{trans} for current along the [100] and [110] directions

In Eqs. (B2) and (B3), the resistivities ρ_{long} and ρ_{trans}, respectively, are given as a function of the angle α between $\boldsymbol{j}$ and the [100] crystal axis. The equations drastically simplify for current directions along [100] and [110], referring to $\alpha = 0°$ and $\alpha = 45°$, respectively. In both cases, the corresponding expressions for the resistivities take the same form, namely,

$$\rho_{\mathrm{long}} = \rho_0 + \rho_1 m_j^2 + \rho_2 m_n^2 + \rho_3 m_j^4 + \rho_4 m_n^4 + \rho_5 m_j^2 m_n^2, \tag{10}$$

$$\rho_{\mathrm{trans}} = \rho_6 m_n + \rho_7 m_j m_t + \rho_8 m_n^3 + \rho_9 m_j m_t m_n^2. \tag{11}$$

All resistivity parameters ρ_i $(i = 0, \ldots, 9)$ are linear combinations of the expansion parameters $A, B, C_1, \ldots$, as specified in Eqs. (B4) and (B5) for $\boldsymbol{j} \| [100]$ and $\boldsymbol{j} \| [110]$, respectively. The parameter ρ_0 in Eq. (10) may be regarded as a reference for the angular dependence of ρ_{long}. It represents the longitudinal resistivity for parallel alignment between $\boldsymbol{m}$ and $\boldsymbol{t}$, where $m_j = m_n = 0$. The reference direction $\boldsymbol{t}$ can be easily changed to $\boldsymbol{j}$ or $\boldsymbol{n}$ by substituting m_j or m_n, respectively, with the help of Eq. (9).

3. Polar plots of ρ_{long} and ρ_{trans}

In order to graphically illustrate the dependence of ρ_{long} and ρ_{trans} on the magnetization orientation $\boldsymbol{m}$, it is instructive to set either m_n, m_j, or m_t in Eqs. (10) and (11) equal to zero and to display the resulting analytical expressions for ρ_{long} and ρ_{trans} in polar plots.

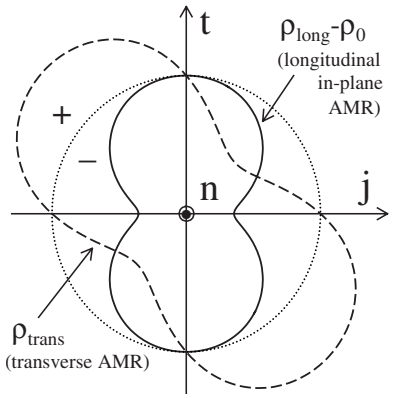

FIG. 1. Schematic polar plot in arbitrary units showing the dependence of $\rho_{\text{long}}-\rho_0$ (solid line) and ρ_{trans} (dashed line) on $\boldsymbol{m}$ for in-plane magnetization perpendicular to $\boldsymbol{n}$. The dotted circle indicates the zero line that separates negative and positive values of $\rho_{\text{long}}-\rho_0$ and ρ_{trans}.

For in-plane magnetization, the identity $m_n=0$ holds and Eqs. (10) and (11) simplify to

$$\rho_{\text{long}} = \rho_0 + \rho_1 m_j^2 + \rho_3 m_j^4, \tag{12}$$

$$\rho_{\text{trans}} = \rho_7 m_j m_t. \tag{13}$$

In Fig. 1, the angular dependence of $\rho_{\text{long}}-\rho_0$ is depicted by the solid line, clearly reflecting the longitudinal in-plane AMR, i.e., the variation of ρ_{long} with the magnetization orientation. The dashed line illustrates the angular dependence of ρ_{trans} and reflects the transverse AMR. The roots of $\rho_{\text{long}}-\rho_0$ and ρ_{trans} are given by the intersection points of the solid and dashed lines, respectively, and the dotted zero line separating the negative and positive values of $\rho_{\text{long}}-\rho_0$ and ρ_{trans}.

An orientation of the magnetization perpendicular to the current direction is equivalent to the condition $m_j=0$. In this case, Eqs. (10) and (11) reduce to

$$\rho_{\text{long}} = \rho_0 + \rho_2 m_n^2 + \rho_4 m_n^4, \tag{14}$$

$$\rho_{\text{trans}} = \rho_6 m_n + \rho_8 m_n^3. \tag{15}$$

The corresponding polar plots of $\rho_{\text{long}}-\rho_0$ and ρ_{trans} in Fig. 2 reflect the longitudinal out-of-plane AMR for $\boldsymbol{m}\perp\boldsymbol{j}$ and the AHE, respectively. In the special case of cubic crystal symmetry and $\boldsymbol{j}\parallel[100]$, Eq. (14) further reduces to

$$\rho_{\text{long}} = \rho_0 + \rho_2 m_t^2 m_n^2 \tag{16}$$

since $\rho_4=-\rho_2$ (see Appendix B). As demonstrated by the dash-dotted line in Fig. 2, ρ_{long} now exhibits fourfold symmetry.

The case $\boldsymbol{m}\perp\boldsymbol{t}$, or equivalently $m_t=0$, is illustrated in Fig. 3, where the solid line again describes the longitudinal out-of-plane AMR and the dashed line the AHE. The appropriate equations for ρ_{long} and ρ_{trans} read as

$$\rho_{\text{long}} = \rho_0 + \rho_1 m_j^2 + \rho_2 m_n^2 + \rho_3 m_j^4 + \rho_4 m_n^4 + \rho_5 m_j^2 m_n^2, \tag{17}$$

$$\rho_{\text{trans}} = \rho_6 m_n + \rho_8 m_n^3. \tag{18}$$

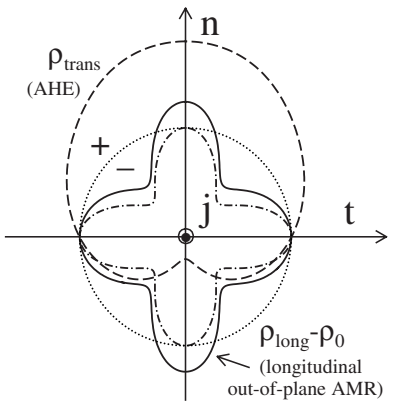

FIG. 2. Dependence of $\rho_{\text{long}}-\rho_0$ (solid line) and ρ_{trans} (dashed line) on $\boldsymbol{m}$ for out-of-plane magnetization perpendicular to $\boldsymbol{j}$. The dash-dotted line illustrates the special case of cubic crystal symmetry and current along [100]. The dotted circle indicates the zero line that separates negative and positive values of $\rho_{\text{long}}-\rho_0$ and ρ_{trans}.

4. Anomalous and ordinary Hall effect

The AHE manifests itself in a contribution to ρ_{trans}, which is linear proportional to the normal component of $\boldsymbol{M}$. It reads as

$$\rho_{\text{trans,AHE}} = (\gamma_1 \rho_{\text{long}} + \gamma_2 \rho_{\text{long}}^2) M m_n, \tag{19}$$

where the linear and quadratic terms in ρ_{long} are usually attributed to the skew scattering and the side-jump scattering mechanisms, respectively.[10,11] A disorder-independent quadratic contribution has also been proposed to arise from Berry phase effects.[12] The experimental results presented in Sec. IV show that $\rho_0 \gg \rho_1, .., \rho_5$, and therefore, as a good approximation, ρ_{long} can be replaced by ρ_0 in Eq. (19). Identifying ρ_6 with $(\gamma_1\rho_0+\gamma_2\rho_0^2)M$, the model presented in this paper properly describes the AHE in a phenomenological way. However, information on the specific contributions of the linear and quadratic terms to ρ_{trans}, quantified by the weighting coefficients γ_1 and γ_2, cannot be inferred from experiment within the framework of the model.

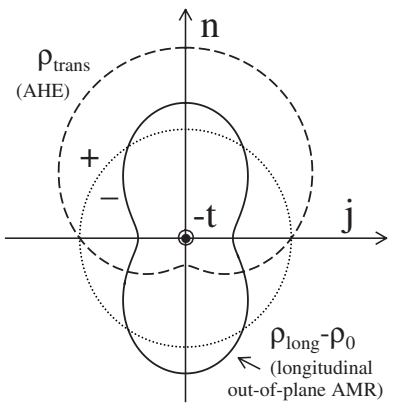

FIG. 3. Schematic polar plot in arbitrary units showing the dependence of $\rho_{\text{long}}-\rho_0$ (solid line) and ρ_{trans} (dashed line) on $\boldsymbol{m}$ for out-of-plane magnetization perpendicular to $\boldsymbol{t}$. The dotted circle indicates the zero line that separates negative and positive values of $\rho_{\text{long}}-\rho_0$ and ρ_{trans}.

In Eq. (2), the resistivity tensor is expanded with respect to the components of $\boldsymbol{M}$. Therefore, the expressions for ρ_{trans} do not account for the ordinary Hall effect, which is related to the magnetic induction $\boldsymbol{B}$. For magnetic field strengths $\mu_0 H < 1$ T and hole concentrations $p > 10^{20}$ cm^{-3} as in our experiments, however, the contribution of the ordinary Hall effect $\mu_0 H/ep$ (where e denotes the elementary charge) to ρ_{trans} is smaller than 6×10^{-6} Ω cm and thus about 2 orders of magnitude smaller than the measured peak values of ρ_{trans} (see Sec. IV). Other effects correlated with $\boldsymbol{B}$, such as the negative magnetoresistance, may be taken into account by considering B-dependent resistivity parameters.

5. Polycrystalline materials

In the literature, the longitudinal in-plane AMR and the transverse AMR in (Ga,Mn)As are often theoretically described by[29,30]

$$\rho_{\mathrm{long}} = \rho_{\perp} + (\rho_{\parallel} - \rho_{\perp})\cos^2 \phi, \tag{20}$$

$$\rho_{\mathrm{trans}} = (\rho_{\parallel} - \rho_{\perp})\sin \phi \cos \phi, \tag{21}$$

where ϕ denotes the angle between $\boldsymbol{j}$ and $\boldsymbol{m}$. Taking into account the relations $\cos^2 \phi = m_j^2$ and $\sin \phi \cos \phi = m_j m_t$, which are only valid for an in-plane configuration, it becomes clear that Eq. (20) is a good approximation to Eq. (12) only if the fourth-order term $\rho_3 m_j^4$ is negligibly small compared to $\rho_1 m_j^2$, i.e., if $|\rho_3| \ll |\rho_1|$ or more generally $|E_1| \ll |C_1|, |C_2|$. The results presented in Sec. IV B reveal that these inequalities do not apply to any of the (Ga,Mn)As samples under study. On the other hand, the angular dependence of ρ_{trans} described by Eq. (21) agrees with that given by Eq. (13). The prefactors of the $\cos^2 \phi$ and $\sin \phi \cos \phi$ terms, however, are in general different and equal only in the special case, where $\rho_1 = \rho_7$, or equivalently, $C_1 = C_2$. As already pointed out in Ref. 25, Eqs. (20) and (21) only apply to isotropic materials such as polycrystals where the resistivities do not depend on the direction $\boldsymbol{j}$ of the current relative to the crystal axes. In fact, Eqs. (20) and (21) result from Eqs. (1) and (4) by averaging over all possible spatial orientations of the coordinate system $\{\boldsymbol{j}, \boldsymbol{t}, \boldsymbol{m}\}$ with respect to the cubic crystal axes.[31] Calculation yields

$$\rho_{\perp} = A + \frac{1}{5}(C_1 - C_2) + \frac{1}{35}(3E_1 + 3E_2 - E_3),$$

$$\rho_{\parallel} - \rho_{\perp} = \frac{1}{5}(2C_1 + 3C_2) + \frac{1}{35}(12E_1 - 2E_2 + 3E_3). \tag{22}$$

6. Uniaxial [110] in-plane anisotropy

Recently, Rushforth *et al.*[32] presented an experimental and theoretical study on the components of the in-plane AMR based on

$$\frac{\rho_{\mathrm{long}} - \rho_{\mathrm{av}}}{\rho_{\mathrm{av}}} = C_I \cos 2\phi + C_U \cos 2\psi + C_C \cos 4\psi + C_{I,C} \cos(4\psi - 2\phi), \tag{23}$$

$$\frac{\rho_{\mathrm{trans}}}{\rho_{\mathrm{av}}} = C_I \sin 2\phi - C_{I,C} \sin(4\psi - 2\phi), \tag{24}$$

which were obtained by extending the model of Döring,[33] introduced for cubic Ni, to systems with cubic [100] plus uniaxial [110] anisotropy. Here, ϕ again denotes the angle between $\boldsymbol{j}$ and $\boldsymbol{m}$, and ψ the angle between $\boldsymbol{m}$ and the [110] crystal direction. The coefficients C_I, C_U, C_C, and $C_{I,C}$ represent a noncrystalline, a uniaxial, a cubic, and a crossed noncrystalline/crystalline contribution, respectively. ρ_{av} is the average value of ρ_{long} as $\boldsymbol{M}$ is rotated through 360°. Starting from Eqs. (B2) and (B3) with $m_n = 0$, it can be shown that the coefficients C_I, C_C, $C_{I,C}$, and ρ_{av} are related to the parameters A, C_1, C_2, and E_1, introduced in Sec. III A, by

$$C_I = \frac{1}{4\rho_{\mathrm{av}}}(C_1 + C_2 + E_1), \quad C_C = -\frac{1}{8\rho_{\mathrm{av}}}E_1,$$

$$C_{I,C} = -\frac{1}{4\rho_{\mathrm{av}}}(C_1 - C_2 + E_1),$$

$$\rho_{\mathrm{av}} = A + \frac{1}{2}C_1 + \frac{3}{8}E_1. \tag{25}$$

In our model no uniaxial [110] anisotropy of the resistivity has been taken into account, i.e., $C_U = 0$, since no significant influence of such a contribution has been found in analyzing the angle-dependent magnetotransport data. This is consistent with the fact that the strength of the magnetic uniaxial in-plane anisotropy (for definition, see Sec. III B), inferred from the experimental data, turned out to be negligibly small in the (Ga,Mn)As samples under study. A uniaxial in-plane contribution may become important, however, when the experiments are performed at temperatures much higher than 4.2 K,[21] when the thickness of the (Ga,Mn)As sample is small,[32] or a uniaxial in-plain strain is induced by a piezoelectric actuator mounted onto the sample.[34,35] The incorporation of the contribution $C_U \cos 2\psi$ from Eq. (23) into our model would yield a further term in the expression of ρ_{long} in Eq. (10). For $\boldsymbol{j} \parallel [100]$, it reads as $\rho_u m_j m_t$ and leads to an additional angular dependence of ρ_{long}. For $\boldsymbol{j} \parallel [110]$, it is given by $-\rho_u/2 + \rho_u m_j^2$ and can be incorporated into the terms ρ_0 and $\rho_1 m_j^2$.

B. Magnetic anisotropy

In Sec. IIA, analytical expressions for ρ_{long} and ρ_{trans} as a function of the magnetization orientation $\boldsymbol{m}$ have been derived. The direction of $\boldsymbol{m}$, in turn, is determined by the MA of the ferromagnetic material and by the strength and orientation of an external magnetic field $\boldsymbol{H}$. Magnetic anisotropy stands for the dependence of the free energy density F of a magnetic system on the orientation of $\boldsymbol{M}$. In addition to supposing a simple single-domain model, we assume that the magnitude M of the magnetization is nearly constant under the given experimental conditions. Instead of F, we therefore consider the normalized quantity $F_M = F/M$, allowing for a more concise description of the MA. For a (Ga,Mn)As film with tetragonal distortion along [001], the anisotropic part of F_M can be written as[19,25]

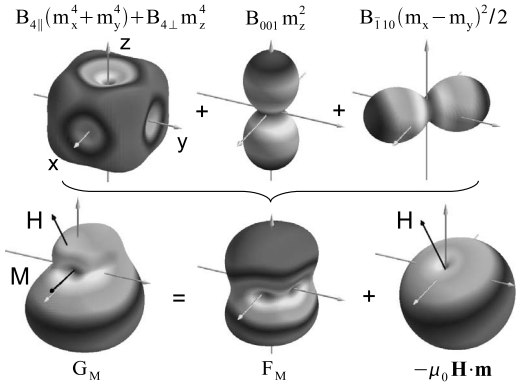

FIG. 4. Graphical illustration of the different contributions to the normalized density of the free enthalpy G_M, plotted as three-dimensional functions of the magnetization orientation. The equilibrium position of $\boldsymbol{M}$ is determined by the minimum of G_M.

$$F_M(\boldsymbol{m}) = B_{4\parallel}(m_x^4 + m_y^4) + B_{4\perp}m_z^4 + B_{2\perp}m_z^2 + \frac{\mu_0 M}{2}m_z^2 + \frac{B_{\bar{1}10}}{2}(m_x - m_y)^2. \quad (26)$$

The first three terms are intrinsic contributions arising from spin-orbit coupling in the valence band. The fourth and fifth terms are extrinsic contributions describing the demagnetization energy of an infinite plane (shape anisotropy) and a uniaxial in-plane contribution, respectively, whose origin is still under discussion.[21,23,36] The two m_z^2 terms cannot be distinguished in our experiments and are therefore lumped into a single term $B_{001}m_z^2$.

In the presence of an external magnetic field $\boldsymbol{H}$, one has to additionally take into account the Zeeman energy, and the total energy density is finally given by the (normalized) free enthalpy density,

$$G_M(\boldsymbol{m}) = F_M(\boldsymbol{m}) - \mu_0 \boldsymbol{H}\cdot\boldsymbol{m}. \quad (27)$$

Figure 4 shows a graphical illustration of the various contributions to G_M. Given an arbitrary magnitude and orientation of the magnetic field $\boldsymbol{H}$, the direction of the magnetization $\boldsymbol{M}$ is determined by the minimum of G_M with respect to the components of $\boldsymbol{m}$.

IV. RESULTS AND DISCUSSION

For sufficiently high magnetic fields, the contribution of the free energy F_M to the free enthalpy G_M in Eq. (27) becomes much smaller than the contribution of the Zeeman energy and can, as a good approximation, be neglected. In this case, the magnetization $\boldsymbol{M}$ aligns with $\boldsymbol{H}$ and the dependence of ρ_{long} and ρ_{trans} on the magnetization orientation can be simply probed by systematically varying the direction of $\boldsymbol{H}$. The values of the resistivity parameters ρ_i are then derived by fitting Eqs. (10) and (11) to the measured data with the vector components of $\boldsymbol{m}$ replaced by those of $\boldsymbol{h}$. When the magnetic field is gradually lowered, however, the Zeeman term in Eq. (27) decreases, the relative contribution of F_M to G_M increases, and the orientation of $\boldsymbol{M}$ more and more deviates from the direction of $\boldsymbol{H}$ toward one of the easy axes

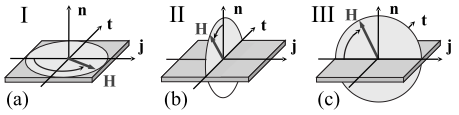

FIG. 5. The angular dependence of the resistivities was probed by rotating an external magnetic field $\boldsymbol{H}$ within three different planes (a) perpendicular to $\boldsymbol{n}$, (b) perpendicular to $\boldsymbol{j}$, and (c) perpendicular to $\boldsymbol{t}$. The corresponding configurations are referred to as I, II, and III, respectively.

determined by the minima of F_M. In other words, the measured resistivities are increasingly influenced by the MA. In Ref. 25, we have shown that this effect can be utilized to probe the MA in (Ga,Mn)As by means of angle-dependent magnetotransport measurements.

In our experimental setup, the field strength of the electromagnet is limited to 0.68 T. In most cases, this value suffices to align $\boldsymbol{M}$ almost perfectly along $\boldsymbol{H}$. In situations, however, where $\boldsymbol{H}$ approaches a hard magnetic axis, this might no longer apply and the influence of the MA has to be taken into account when deriving resistivity parameters from angle-dependent resistivity curves. Therefore, we routinely determined both resistivity and anisotropy parameters for all samples under study. The corresponding procedure is exemplified in Sec. IV A by means of an almost unstrained (Ga,Mn)As layer with $\varepsilon_{zz}=-0.04\%$. In Sec. IV B, the strain dependence of the resistivity parameters ρ_i will be discussed. An analogous study on the anisotropy parameters B_i goes beyond the scope of this paper and will be presented elsewhere. A brief survey, however, is given in Ref. 24.

A. Determination of the resistivity parameters

The longitudinal and transverse resistivities of the (Ga,Mn)As layers were measured for both $\boldsymbol{j}\parallel[100]$ and $\boldsymbol{j}\parallel[110]$ as a function of the magnetic field orientation at fixed field strengths of $\mu_0 H=0.11$, 0.26, and 0.65 T. At each field strength, $\boldsymbol{H}$ was rotated within three different crystallographic planes perpendicular to $\boldsymbol{n}$, $\boldsymbol{j}$, and $\boldsymbol{t}$, respectively. The corresponding configurations, labeled I, II, and III, are shown in Fig. 5. In the case of $\boldsymbol{M}\parallel\boldsymbol{H}$, they are identical to the configurations used in Figs. 1–3 to illustrate the theoretical angular dependences of ρ_{long} and ρ_{trans} by means of schematic polar plots.

Prior to each angular scan, the magnetization $\boldsymbol{M}$ was put into a clearly defined initial state by raising the field to its maximum value of 0.68 T, where $\boldsymbol{M}$ is supposed to nearly saturate and to align with the external field. The field was then lowered to one of the above mentioned magnitudes and the scan was started. Figures 6 and 7 show as an example the angular dependences of ρ_{long} and ρ_{trans} for the almost unstrained sample with $\varepsilon_{zz}=-0.04\%$, measured for $\boldsymbol{j}$ along [100] and [110], respectively.

The experimental data are depicted by the red solid circles. In the first case, $\boldsymbol{H}$ was rotated in the (001), (100), and (010) planes, and in the second case, the planes of rotation were the (001), (110), and $(\bar{1}10)$ planes, corresponding to configurations I, II, and III, respectively. At 0.65 T, the Zeeman energy dominates the free enthalpy. Consequently,

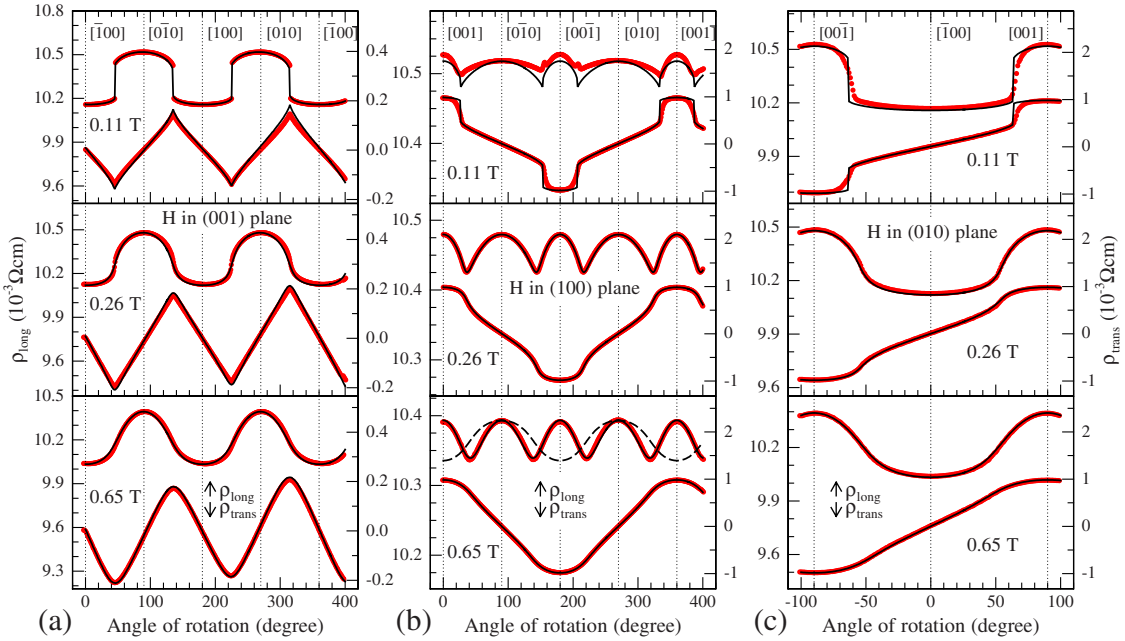

FIG. 6. (Color online) Resistivities ρ_{long} and ρ_{trans} recorded from the nearly unstrained (Ga,Mn)As layer with $\varepsilon_{zz}=-0.04\%$ at 4.2 K and $\boldsymbol{j}\|[100]$ (red solid circles). The measurements were carried out at fixed field strengths of $\mu_0 H=0.11$, 0.26, and 0.65 T with $\boldsymbol{H}$ rotated in (a) the (001), (b) the (100), and (c) the (010) plane, corresponding to configurations I, II, and III, respectively. The black solid lines are fits to the experimental data using Eqs. (10) and (11) and one single set of resistivity and anisotropy parameters. The dashed line in (b) at 0.65 T represents an attempt to fit the measured curve considering only terms up to the second order.

$\boldsymbol{M}$ nearly aligns with $\boldsymbol{H}$ and continuously follows its motion. In fact, the curves of ρ_{long} and ρ_{trans} at 0.65 T are smooth and largely reflect the angular dependences of the resistivities described by Eqs. (10) and (11) with $\boldsymbol{m}$ replaced by $\boldsymbol{h}$. With decreasing magnetic field the influence of the MA increases and the orientation of $\boldsymbol{M}$ deviates more and more from the field direction. Accordingly, jumps and kinks occur in the curves at 0.26 and 0.11 T, arising from sudden movements of $\boldsymbol{M}$ caused by discontinuous displacements of the minimum of G_M.

Values for the resistivity parameters ρ_i and the anisotropy parameters B_i were determined by an iterative fit procedure. Starting with an initial guess for the anisotropy parameters, the resistivity parameters were obtained by fitting Eqs. (10)

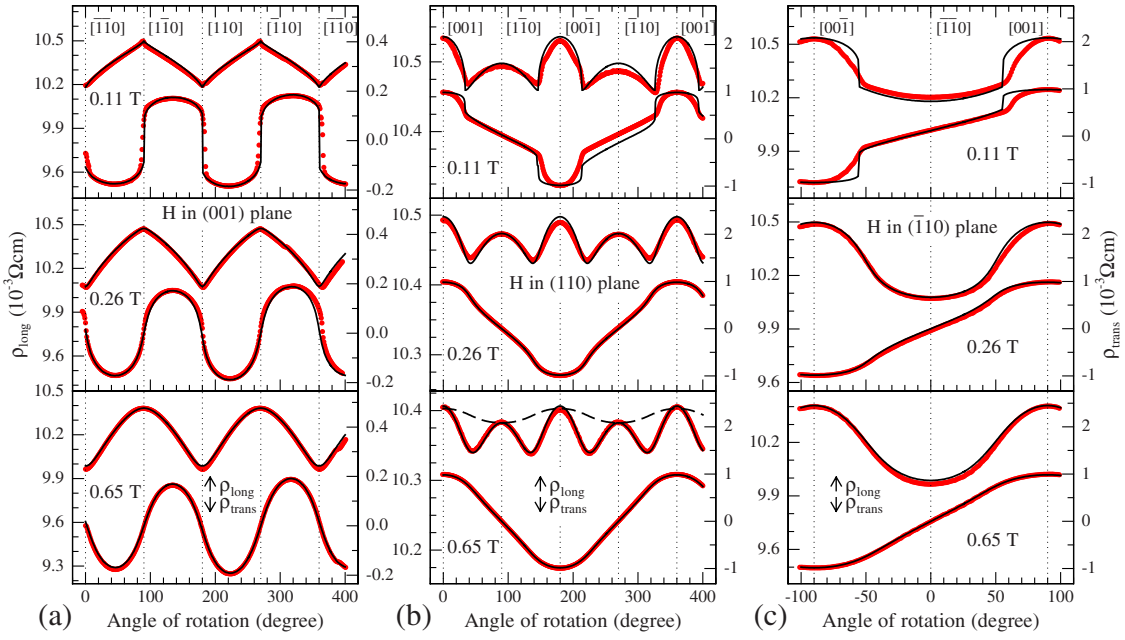

FIG. 7. (Color online) Continuation from Fig. 6. The current direction is now along [110] and the magnetic field $\boldsymbol{H}$ was rotated in (a) the (001), (b) the (110), and (c) the $(\bar{1}10)$ plane, corresponding to configurations I, II, and III, respectively.

TABLE I. Values of the resistivity parameters in units of 10^{-4} Ω cm determined for the nearly unstrained (Ga,Mn)As layer with $\varepsilon_{zz}=-0.04\%$.

ρ_i (10^{-4} Ω cm)	$\boldsymbol{j}\parallel[100]$	$\boldsymbol{j}\parallel[110]$
ρ_0 (0.65 T)	103.9	103.8
ρ_0 (0.26 T)	104.8	104.7
ρ_0 (0.11 T)	105.2	105.1
ρ_1	−5.3	−2.3
ρ_2	−2.2	−1.9
ρ_3	1.7	−1.7
ρ_4	2.2	2.2
ρ_5	2.2	−0.4
ρ_6	9.8	9.8
ρ_7	−4.0	−3.6
ρ_8	0.0	0.0
ρ_9	1.3	0.5

and (11) to the experimental data recorded at 0.65 T. Then, the anisotropy parameters were modified for an optimal agreement at 0.26 and 0.11 T, and the whole procedure was repeated until no further improvement of the fit could be achieved. The unit vector $\boldsymbol{m}$, whose components enter Eqs. (10) and (11), was calculated for any given magnetic field $\boldsymbol{H}$ by numerically minimizing G_M with respect to the direction of $\boldsymbol{m}$.

With the exception of ρ_0, the resistivity parameters were assumed to be field independent, which turned out to be a good approximation within the accuracy of the fit. ρ_0 was found to decrease with increasing magnetic field, reflecting the negative-magnetoresistance behavior of ρ_{long}. The values of the resistivity parameters for $\boldsymbol{j}\parallel[100]$ and $\boldsymbol{j}\parallel[110]$, obtained from the fits, are listed in Table I. The two sets of parameters are related to each other according to Eqs. (B8) and (B9), in agreement with the theoretical model presented in Sec. III. The parameter ρ_9 is not immediately accessible by measurements performed in configurations I, II, and III since the corresponding term in Eq. (11) vanishes in all the three cases. It can be determined, however, either directly by orienting $\boldsymbol{H}$ in a way that m_j, m_t, and m_n are all different from zero or indirectly by using the relation $\rho_9'=\rho_5-\rho_3$, where the primed and unprimed parameters correspond to $\boldsymbol{j}\parallel[100]$ and $\boldsymbol{j}\parallel[110]$, respectively, and vice versa (see Appendix B). For the anisotropy parameters, we obtained the values $B_{4\parallel}=B_{4\perp}=-35$ mT, $B_{001}=35$ mT, and $B_{\bar{1}10}=-5$ mT. The theoretical curves calculated with these parameters are drawn as the solid lines in Figs. 6 and 7.

For $\mu_0 H=0.26$ and 0.65 T, an excellent agreement between the measured and simulated curves is achieved, while for $\mu_0 H=0.11$ T, significant differences emerge. We interpret these differences as clear evidence for the gradual breakdown of the single-domain model with constant magnetization magnitude M at low magnetic fields. The experimental curves recorded in configurations II and III at 0.11 T are much smoother than the calculated ones, probably reflecting the formation of a multitude of differently oriented ferromagnetic domains. This interpretation is supported by a number of investigations visualizing the domain structure of (Ga,Mn)As layers at low magnetic fields[37–41] as well as by further magnetotransport measurements on the (Ga,Mn)As samples under study, not presented in this paper. Remarkably, the theoretical curves in Figs. 6(a) and 7(a), calculated for configuration I where $\boldsymbol{H}$ is rotated in the (001) layer plane, almost perfectly describe the measured curves even at 0.11 T. This may be explained by the fact that due to shape anisotropy the [001] axis perpendicular to the surface is a hard axis even in the unstrained layer and that, as a consequence, ferromagnetic domains with in-plane magnetization remain more stable at low magnetic fields than domains with out-of-plane magnetization. Accordingly, the jumps and kinks in Figs. 6(a) and 7(a) at 0.11 T are extremely well pronounced, reflecting nearly perfect coherent switching of the whole spin system.

Whereas the measured resistivity curves presented in Ref. 25 for two (Ga,Mn)As layers, grown on GaAs(001) and GaAs(113) substrates, could be satisfactorily well fitted by the analytical expressions containing only terms up to the second order in the components of $\boldsymbol{m}$, it is now compulsory to take into account higher-order terms. In order to illustrate the importance of the fourth-order terms for a correct description of the experimental traces of ρ_{long}, simulations are depicted as the dashed lines in Figs. 6(b) and 7(b) where only the terms up to the second order in m_i were considered. No matter which values for ρ_2 in Eq. (10) were chosen, the model curves completely failed to reproduce the measured angular dependence of ρ_{long}.

B. Strain dependence of the resistivity parameters

It is well known that a distortion of the (Ga,Mn)As crystal lattice leads to a significant change of the MA. Microscopically, this can be explained by a strain-induced warping of the valence bands in addition to that caused by spin-orbit coupling.[14] The warping, however, affects not only the MA but also the AMR and thus the resistivity parameters ρ_i.

In order to examine the influence of the vertical strain ε_{zz} on ρ_{long} and ρ_{trans}, angle-dependent magnetotransport measurements analogous to those presented in Figs. 6 and 7 were performed on all (Ga,Mn)As samples under study. Using the procedure described in Sec. IV A, the resistivity parameters $\rho_0,\ldots,\rho_8$ for $\boldsymbol{j}\parallel[100]$ and $\boldsymbol{j}\parallel[110]$ were determined independently of each other without taking into account their mutual relations theoretically predicted by Eqs. (B8) and (B9). Whereas the values obtained for ρ_0 randomly scatter in the range from 5.0×10^{-3} to 8.8×10^{-3} Ω cm, presumably due to variations in the hole concentration and mobility, a distinct correlation with the strain is found for the other resistivity parameters. This correlation is seen most clearly by considering the normalized quantities ρ_i/ρ_0 instead of ρ_i. In Fig. 8, the values of ρ_i/ρ_0 ($i=1,\ldots,8$) are plotted against ε_{zz} in the range $-0.46\%\leq\varepsilon_{zz}\leq0.22\%$ for $\boldsymbol{j}\parallel[100]$ and $\boldsymbol{j}\parallel[110]$. The parameter ρ_9 (not shown) was determined by the indirect method described above and turned out to be nearly independent of the strain with $\rho_9/\rho_0\approx0.015$ for $\boldsymbol{j}\parallel[100]$ and $\rho_9/\rho_0\approx0$ for $\boldsymbol{j}\parallel[110]$.

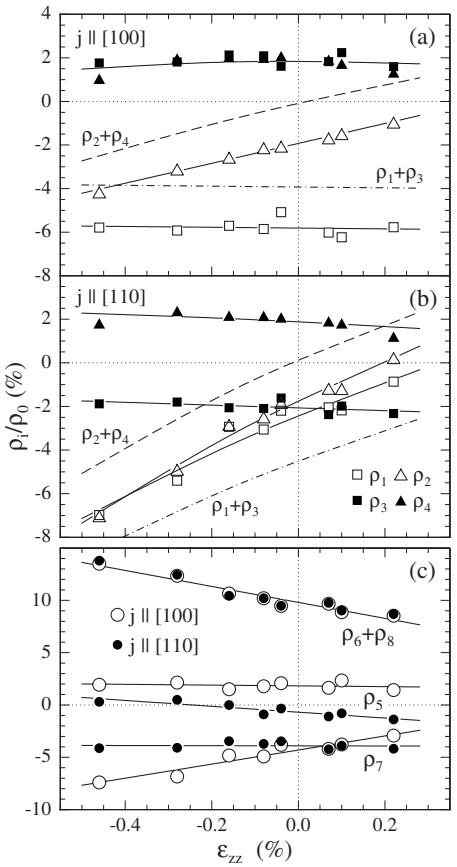

FIG. 8. Values of the normalized resistivity parameters ρ_i/ρ_0 $(i=1,\ldots,8)$ plotted against the vertical strain ε_{zz}. The solid lines are smoothing splines and are drawn to guide the eye. In (a) the normalized values of $\rho_1,\ldots,\rho_4$ are shown for $\boldsymbol{j}\|[100]$ and in (b) for $\boldsymbol{j}\|[110]$. The dash-dotted and dashed lines depict the strain dependence of $\rho_1+\rho_3$ and $\rho_2+\rho_4$, respectively, and are obtained by adding the individual spline curves. In (c), the normalized values of ρ_5, $\rho_6+\rho_8$, and ρ_7 are shown for both current directions.

According to our theoretical model, the resistivity parameters for $\boldsymbol{j}\|[100]$ and $\boldsymbol{j}\|[110]$ should be linearly related to each other by Eqs. (B8) and (B9), yielding, for instance, the symmetrical relations

$$\rho_1' = \rho_3 + \rho_7, \quad \rho_8' = \rho_8,$$

$$\rho_3' = -\rho_3, \quad \rho_7' = \rho_1 + \rho_3, \quad \rho_6' = \rho_6, \tag{28}$$

The primed and unprimed parameters correspond to the current directions [110] and [100], respectively, and vice versa. Inspection of Fig. 8 reveals that the measured data comply with the above relations supporting the validity of the theoretical model.

In contrast to the resistivity parameters ρ_i, the expansion parameters $B, C_1, \ldots, e_4$ do not depend on the current direction and have thus a more fundamental meaning. They can be unambiguously calculated from the resistivity parameters using Eqs. (B4) and (B5). If ρ_9 is measured directly, only one set of resistivity parameters is needed; otherwise, the ρ_i have to be known for both current directions, $\boldsymbol{j}\|[100]$ and $\boldsymbol{j}\|[110]$. In this work, the second case applies. Figure 9 shows the

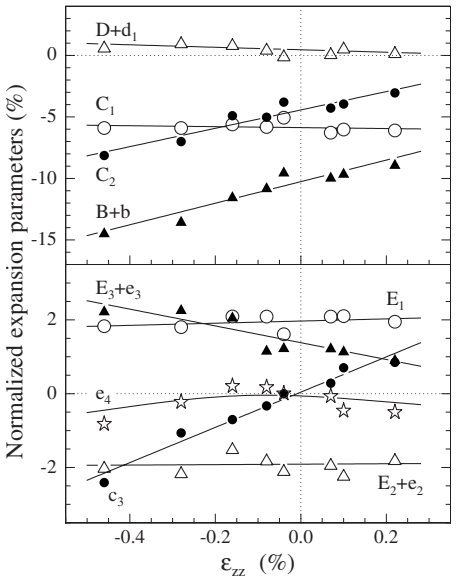

FIG. 9. Expansion parameters $B+b,\ldots,e_4$ plotted against the vertical strain ε_{zz}. The values were calculated from ρ_i $(i=1,\ldots,8)$ using Eqs. (B4) and (B5) and are normalized to that of A. The solid lines are smoothing splines and are drawn to guide the eye.

values of the expansion parameters normalized to A in dependence on the vertical strain ε_{zz}. The smoothing spline curves suggest that the parameters related to the cubic part $\bar{\rho}_{\text{cubic}}$ of the resistivity tensor (capital letters) as well as the parameters appearing in the strain-induced difference term $\Delta\bar{\rho}$ (small letters) almost linearly vary with ε_{zz} in agreement with Eq. (7).

The variation of the resistivity parameters with the strain manifests itself in a pronounced change of the angular dependences of ρ_{long} and ρ_{trans}. This is exemplarily demonstrated in Figs. 10 and 11, where the normalized resistivities $(\rho_{\text{long}}-\rho_0)/\rho_0$ and $\rho_{\text{trans}}/\rho_0$, respectively, at $\mu_0 H=0.65$ T are plotted as a function of the magnetic field orientation and the strain for some of the configurations presented in Figs. 6 and 7.

The experimental data are again depicted by the red solid circles and the calculated curves by the black solid lines. In Fig. 10(a), the longitudinal resistivity measured in configuration I is shown for $\boldsymbol{j}\|[110]$. Provided that $\boldsymbol{M}$ and $\boldsymbol{H}$ are approximately parallel to each other at 0.65 T, the angle-dependent oscillations of ρ_{long} reflect the longitudinal in-plane AMR illustrated in Fig. 1. The amplitude of the oscillations is given by $\rho_1+\rho_3$ and increases with decreasing compressive and increasing tensile strain. It is depicted by the dash-dotted line in Fig. 8(b). The specific shape of the oscillations is determined by the ratio of ρ_1 and ρ_3 representing the m_j^2 and m_j^4 terms, respectively. As shown in Fig. 8(b), ρ_1 strongly varies with ε_{zz}, whereas ρ_3 remains nearly constant. Figure 8(a) reveals that for $\boldsymbol{j}\|[100]$, ρ_1, ρ_3, and $\rho_1+\rho_3$ are almost independent of the strain. Accordingly, the longitudinal in-plane AMR is almost constant and the corresponding curves of ρ_{long} are nearly identical (not shown). It should be noted again that for all samples under study, the condition $|\rho_3| \ll |\rho_1|$ does not apply and thus Eq. (20) fails to correctly describe the angular dependence of ρ_{long}.

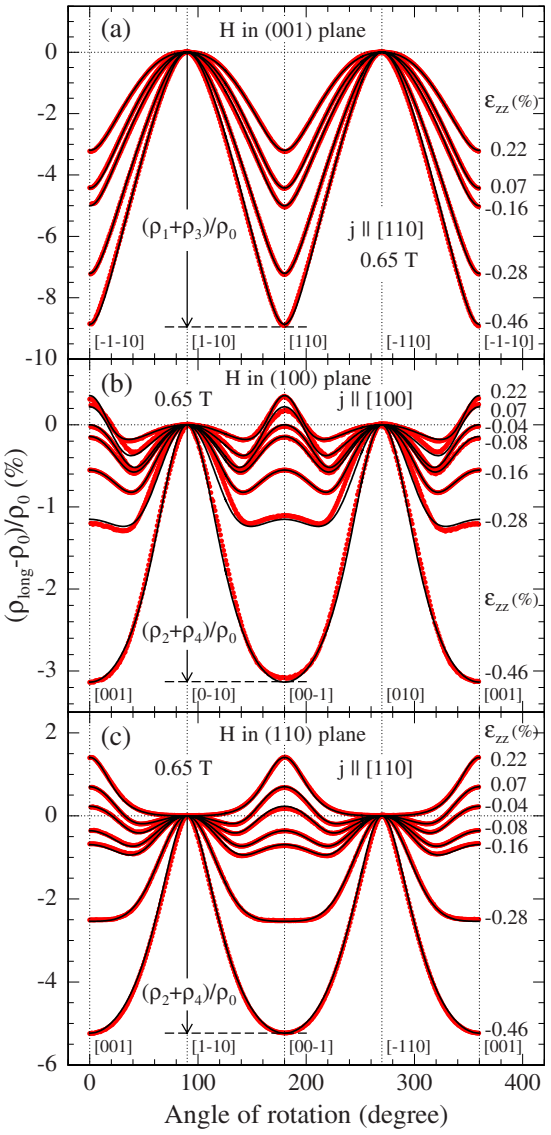

FIG. 10. (Color online) Variation of the angle-dependent normalized longitudinal resistivity $(\rho_{long}-\rho_0)/\rho_0$ with vertical strain ε_{zz} at $\mu_0 H=0.65$ T and $T=4.2$ K. The resistivity was recorded as a function of the magnetic field orientation for (a) $\boldsymbol{j}\|[110]$ and $\boldsymbol{H}$ in the (001) plane, (b) $\boldsymbol{j}\|[100]$ and $\boldsymbol{H}$ in the (100) plane, and (c) $\boldsymbol{j}\|[110]$ and $\boldsymbol{H}$ in the (110) plane. The experimental data are depicted by the red solid circles and the calculated curves by the black solid lines.

Whereas for configuration I (see above) and configuration III (not shown), the overall angular dependence of ρ_{long} is basically the same in the whole range of ε_{zz} under investigation, an essential variation with the strain occurs when $\boldsymbol{H}$ and thus $\boldsymbol{M}$ is rotated perpendicular to $\boldsymbol{j}$ (configuration II). In Figs. 10(b) and 10(c), this variation is shown for $\boldsymbol{j}\|[100]$ and $\boldsymbol{j}\|[110]$, respectively. The complex angular dependences emerging for $\varepsilon_{zz}>-0.46\%$, i.e., the appearance of more than two maxima, qualitatively agree with the polar plot depicted in Fig. 2. They result from a competition between the second-order term $\rho_2 m_n^2$ and the fourth-order term $\rho_4 m_n^4$ and occur whenever ρ_2 and ρ_4 are of comparable magnitude and opposite sign, or briefly, whenever $\rho_2+\rho_4$ is close to zero. As

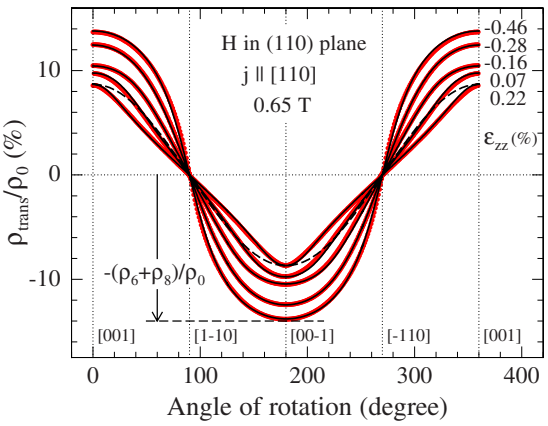

FIG. 11. (Color online) Variation of the angle-dependent normalized transverse resistivity ρ_{trans}/ρ_0 with vertical strain ε_{zz} at $\mu_0 H=0.65$ T and $T=4.2$ K. The resistivity was recorded as a function of magnetic field orientation for $\boldsymbol{j}\|[110]$ and $\boldsymbol{H}$ in the (110) plane. The dashed line was calculated setting all magnetic anisotropy parameters to zero and demonstrates the influence of the MA at 0.65 T for $\varepsilon_{zz}=0.22\%$.

shown by the dashed curves in Figs. 8(a) and 8(b), this applies for $\varepsilon_{zz}>-0.46\%$, in agreement with Figs. 10(b) and 10(c). For both $\boldsymbol{j}\|[100]$ and $\boldsymbol{j}\|[110]$, $\rho_2+\rho_4$ monotonously increases with ε_{zz} and changes sign at the transition from tensile to compressive strain. In the case of $\boldsymbol{j}\|[100]$, symmetry demands that $\rho_2+\rho_4$ exactly equals zero at $\varepsilon_{zz}=0$. The corresponding polar plot is schematically illustrated by the dash-dotted line in Fig. 2.

The evolution of the transverse resistivity with ε_{zz} is exemplarily discussed in Fig. 11, where the angular dependence of ρ_{trans}/ρ_0 is depicted for $\boldsymbol{j}\|[110]$ and $\boldsymbol{m}\perp\boldsymbol{j}$ (configuration II). For magnetization orientation along [001], i.e., perpendicular to the layer plane, ρ_{trans} equals $\rho_6+\rho_8$. As demonstrated in Fig. 8(c), the sum $\rho_6+\rho_8$ is identical for both current directions and linearly decreases with increasing ε_{zz}. In Fig. 9(a), the dependences of $\rho_6=-(B+b)$ and $\rho_8=-(D+d_1)$ on ε_{zz} are displayed as separate curves. They reveal that the values of ρ_6 and ρ_8 have opposite sign and differ by more than 1 order of magnitude. The dominant parameter ρ_6 corresponds to the linear term m_n in Eq. (11), which is usually associated with the AHE. The increasing deviation of the curves in Fig. 11 from a cosinusoidal oscillation for increasing compressive and tensile strain is primarily due to the influence of the magnetic anisotropy even at 0.65 T. For comparison, the resistivity curve calculated for vanishing MA and $\varepsilon_{zz}=0.22\%$ is drawn as a dashed line.

V. SUMMARY

Based on the expansion of the resistivity tensor with respect to the direction cosines of the magnetization up to the fourth order, we have presented a macroscopic analytical model for the longitudinal and transverse resistivities of single-crystalline cubic and tetragonal ferromagnets. The model applies to arbitrary magnetization orientations and current directions. It correctly describes the results of angle-dependent magnetotransport measurements performed on a

series of (Ga,Mn)As layers with a vertical strain gradually varied from tensile to compressive. The resistivity parameters, obtained by fitting Eqs. (10) and (11) to the experimental data, were found to systematically vary with the strain.

ACKNOWLEDGMENTS

This work was supported by the Deutsche Forschungsgemeinschaft under Contract No. Li 988/4.

APPENDIX A: GENERATING SYMMETRY MATRICES AND EXPANSION PARAMETERS

Neumann's principle requires that a tensor representing a macroscopic physical property of a crystal must be invariant under all symmetry operations S of the corresponding point group. The mathematical formulation of this requirement leads to conditional equations for the expansion coefficients $a_{ij}, a_{kij}, \ldots$ of the resistivity tensor in Eq. (2) reading as

$$a_{ij} = S_{io} S_{jp} a_{op}, \quad a_{kij} = |\bar{S}| S_{kq} S_{io} S_{jp} a_{qop},$$

$$a_{klij} = |\bar{S}|^2 S_{kq} S_{lr} S_{io} S_{jp} a_{qrop},$$

$$a_{klmij} = |\bar{S}|^3 S_{kq} S_{lr} S_{mt} S_{io} S_{jp} a_{qrtop},$$

$$a_{klmnij} = |\bar{S}|^4 S_{kq} S_{lr} S_{mt} S_{nu} S_{io} S_{jp} a_{qrtuop}, \tag{A1}$$

where S_{ij} denotes the ij component and $|\bar{S}|$ denotes the determinant of the symmetry matrix $\bar{S}$. The determinant appears in the formula of Eqs. (A1) since $\boldsymbol{M}$ is an axial vector, whereas $\boldsymbol{E}$ and $\boldsymbol{J}$ are polar vectors. In order to derive a complete set of conditional equations for the expansion coefficients, it is sufficient to apply Eq. (A1) to a small set of generating symmetry matrices. In the cases of cubic symmetry T_d and tetragonal symmetry D_{2d}, this set consists of only two matrices, namely, $\bar{S}_8$ and $\bar{S}_9$ and $\bar{S}_2$ and $\bar{S}_8$, respectively. The matrices are given by[28]

$$\bar{S}_2 = \begin{pmatrix} -1 & 0 & 0 \\ 0 & 1 & 0 \\ 0 & 0 & -1 \end{pmatrix}, \quad \bar{S}_8 = \begin{pmatrix} 0 & -1 & 0 \\ 1 & 0 & 0 \\ 0 & 0 & -1 \end{pmatrix},$$

$$\bar{S}_9 = \begin{pmatrix} 0 & 1 & 0 \\ 0 & 0 & 1 \\ 1 & 0 & 0 \end{pmatrix}. \tag{A2}$$

Solving Eqs. (A1) for these generating matrices leads to the resistivity tensors given in Eqs. (4) and (5). The expansion parameters $A, \ldots, E_3$ and $a, \ldots, e_7$ are related to the expansion coefficients $a_{ij}, a_{kij}, \ldots$ by

$$A = a_{11} + a_{1122} + a_{111122}, \quad B = a_{123} + 3a_{12223},$$

$$C_1 = a_{1111} - a_{1122} + 6a_{112211} - 2a_{111122},$$

$$C_2 = 2a_{1212} + 4a_{111212}, \quad D = a_{11123} - 3a_{12223},$$

$$E_1 = a_{111111} - 6a_{112211} + a_{111122},$$

$$E_2 = 6a_{112233} - 2a_{111122}, \quad E_3 = 12a_{112323} - 4a_{111212}. \tag{A3}$$

$$a = a_{33} - a_{11} + a_{1133} - a_{1122} + a_{111133} - a_{111122},$$

$$b = a_{312} - a_{123} + 3a_{11312} - 3a_{12223},$$

$$c_1 = a_{3333} - a_{1111} + a_{1122} - a_{1133} + 6a_{113333} - 6a_{112211} + 2a_{111122} - 2a_{111133},$$

$$c_2 = 2a_{2323} - 2a_{1212} + 4a_{111313} - 4a_{111212},$$

$$c_3 = a_{3311} - a_{1122} + 6a_{113311} - 6a_{112211},$$

$$d_1 = 3a_{12223} - 3a_{11312} + a_{33312} - a_{11123},$$

$$d_2 = 3a_{13323} - 3a_{12223},$$

$$e_1 = a_{333333} - a_{111111} + 6a_{112211} - 6a_{113333} + a_{111133} - a_{111122},$$

$$e_2 = 6a_{113322} - 6a_{112233} + 6a_{112211} - 6a_{113311},$$

$$e_3 = 12a_{123312} - 12a_{112323},$$

$$e_4 = a_{333311} - a_{111122} + 6a_{112211} - 6a_{113311},$$

$$e_5 = 2a_{111122} - 2a_{111133}, \quad e_6 = 4a_{111212} - 4a_{111313},$$

$$e_7 = 4a_{133313} - 4a_{111313}. \tag{A4}$$

APPENDIX B: RESISTIVITY PARAMETERS

To cover the general case of a current flowing along an arbitrary direction within the (001) plane, we write $\boldsymbol{j}$, $\boldsymbol{t}$, and $\boldsymbol{n}$ as

$$\boldsymbol{j} = \begin{pmatrix} \cos\alpha \\ \sin\alpha \\ 0 \end{pmatrix}, \quad \boldsymbol{t} = \begin{pmatrix} -\sin\alpha \\ \cos\alpha \\ 0 \end{pmatrix}, \quad \boldsymbol{n} = \begin{pmatrix} 0 \\ 0 \\ 1 \end{pmatrix}, \tag{B1}$$

where α denotes the angle between the current direction and the [100] crystal axis. Using Eqs. (1), (4), (5), and (8), the resistivities ρ_{long} and ρ_{trans} for tetragonal symmetry can be written as polynomials of fourth order in the variables m_j, m_t, and m_n,

$$\rho_{\text{long}} = A + \left(C_1 - C_2 + \frac{1}{2}E_1\right)\frac{1-\cos 4\alpha}{4} + \left[C_1 - (C_1 - C_2 - E_1)\frac{1-\cos 4\alpha}{2}\right]m_j^2 + \left[c_3 + \tilde{E}_2 - (C_1 - C_2 + E_1 + \tilde{E}_2 + \tilde{E}_3)\frac{1-\cos 4\alpha}{4}\right]m_n^2 + E_1 \cos 4\alpha m_j^4 + \left[-\tilde{E}_2 + e_4 + \left(\frac{1}{2}E_1 + \tilde{E}_2 + \tilde{E}_3\right)\frac{1-\cos 4\alpha}{4}\right]m_n^4 - \left[\tilde{E}_2 + (E_1 - \tilde{E}_2 - \tilde{E}_3)\frac{1-\cos 4\alpha}{2}\right]m_j^2 m_n^2 - \frac{1}{2}(C_1 - C_2)\sin 4\alpha m_j m_t - E_1 \sin 4\alpha m_j^3 m_t + \frac{1}{2}(\tilde{E}_2 + \tilde{E}_3)\sin 4\alpha m_j m_t m_n^2, \quad \text{(B2)}$$

$$\rho_{\text{trans}} = -\tilde{B}m_n + \left[C_2 + (C_1 - C_2 + E_1)\frac{1-\cos 4\alpha}{2}\right]m_j m_t - \tilde{D}m_n^3 + \left[\tilde{E}_3 - (E_1 + \tilde{E}_2 + \tilde{E}_3)\frac{1-\cos 4\alpha}{2}\right]m_j m_t m_n^2 + \frac{1}{4}(C_1 - C_2 + E_1)\sin 4\alpha(m_t^2 - m_j^2) + \frac{1}{4}(E_1 + \tilde{E}_2 + \tilde{E}_3)\sin 4\alpha(m_j^2 - m_t^2)mn^2, \quad \text{(B3)}$$

with the abbreviations $\tilde{B}=B+b$, $\tilde{D}=D+d_1$, $\tilde{E}_2=E_2+e_2$, and $\tilde{E}_3=E_3+e_3$.

For $\boldsymbol{j}\|[100]$ and $\boldsymbol{t}\|[010]$, i.e., $\alpha=0°$, the resistivity parameters ρ_i are given by

$$\rho_0 = A, \quad \rho_1 = C_1, \quad \rho_2 = \tilde{E}_2 + c_3, \quad \rho_3 = E_1,$$

$$\rho_4 = -\tilde{E}_2 + e_4, \quad \rho_5 = -\tilde{E}_2, \quad \rho_6 = -\tilde{B}, \quad \rho_7 = C_2,$$

$$\rho_8 = -\tilde{D}, \quad \rho_9 = \tilde{E}_3, \quad \text{(B4)}$$

and for $\boldsymbol{j}\|[110]$ and $\boldsymbol{t}\|[\bar{1}10]$, i.e., $\alpha=45°$, we obtain

$$\rho_0 = A + \frac{1}{2}[C_1 - C_2] + \frac{1}{4}E_1, \quad \rho_1 = C_2 + E_1,$$

$$\rho_2 = \frac{1}{2}[-C_1 + C_2 + 2c_3 - E_1 + \tilde{E}_2 - \tilde{E}_3], \quad \rho_3 = -E_1,$$

$$\rho_4 = \frac{1}{2}\left[\frac{1}{2}E_1 - \tilde{E}_2 + \tilde{E}_3 + 2e_4\right], \quad \rho_5 = -E_1 + \tilde{E}_3,$$

$$\rho_6 = -\tilde{B}, \quad \rho_7 = C_1 + E_1, \quad \rho_8 = -\tilde{D}, \quad \rho_9 = -E_1 - \tilde{E}_2. \quad \text{(B5)}$$

For unstrained layers with perfect cubic crystal symmetry, the expansion parameters represented by small letters vanish. Then, in the case of $\boldsymbol{j}\|[100]$, the relation

$$\rho_4 = \rho_5 = -\rho_2 \quad \text{(B6)}$$

holds, and for $\boldsymbol{j}\|[110]$, the constraints

$$2\rho_2 = \rho_1 + 3\rho_3 - \rho_5 - \rho_7 - \rho_9,$$

$$4\rho_4 = -5\rho_3 + 2\rho_5 + 2\rho_9 \quad \text{(B7)}$$

apply.

The parameters ρ_i $(i=0,\ldots,9)$ may be thought of as the components of ten-dimensional vectors $\boldsymbol{\rho}$, which for $\boldsymbol{j}\|[100]$ and $\boldsymbol{j}\|[110]$ are related to each other by the linear transformation,

$$\boldsymbol{\rho}_{[110]} = \bar{T} \cdot \boldsymbol{\rho}_{[100]}. \quad \text{(B8)}$$

The matrix T, satisfying the equation $\bar{T}^{-1}=\bar{T}$, is given by

$$\bar{T} = \begin{pmatrix} 1 & \frac{1}{2} & . & \frac{1}{4} & . & . & . & -\frac{1}{2} & . & . \\ . & . & . & 1 & . & . & . & 1 & . & . \\ . & -\frac{1}{2} & 1 & -\frac{1}{2} & . & \frac{1}{2} & . & \frac{1}{2} & . & -\frac{1}{2} \\ . & . & . & -1 & . & . & . & . & . & . \\ . & . & . & \frac{1}{4} & 1 & -\frac{1}{2} & . & . & . & \frac{1}{2} \\ . & . & . & -1 & . & . & . & . & . & 1 \\ . & . & . & . & . & . & 1 & . & . & . \\ . & 1 & . & 1 & . & . & . & . & . & . \\ . & . & . & . & . & . & . & . & 1 & . \\ . & . & . & -1 & . & 1 & . & . & . & . \end{pmatrix}. \quad \text{(B9)}$$

*wolfgang.limmer@uni-ulm.de; http://hlpsrv.physik.uni-ulm.de

[1] H. Ohno, Science **281**, 951 (1998).
[2] A. H. MacDonald, P. Schiffer, and N. Samarth, Nat. Mater. **4**, 195 (2005).
[3] T. Jungwirth, J. Sinova, J. Mašek, J. Kučera, and A. H. MacDonald, Rev. Mod. Phys. **78**, 809 (2006), and references therein.
[4] D. V. Baxter, D. Ruzmetov, J. Scherschligt, Y. Sasaki, X. Liu, J. K. Furdyna, and C. H. Mielke, Phys. Rev. B **65**, 212407 (2002).

[5] T. Jungwirth, J. Sinova, K. Y. Wang, K. W. Edmonds, R. P. Campion, B. L. Gallagher, C. T. Foxon, Q. Niu, and A. H. MacDonald, Appl. Phys. Lett. **83**, 320 (2003).
[6] F. Matsukura, M. Sawicki, T. Dietl, D. Chiba, and H. Ohno, Physica E (Amsterdam) **21**, 1032 (2004).
[7] S. T. B. Goennenwein, S. Russo, A. F. Morpurgo, T. M. Klapwijk, W. Van Roy, and J. De Boeck, Phys. Rev. B **71**, 193306 (2005).
[8] K. Y. Wang, K. W. Edmonds, R. P. Campion, L. X. Zhao, C. T. Foxon, and B. L. Gallagher, Phys. Rev. B **72**, 085201 (2005).
[9] H. X. Tang, R. K. Kawakami, D. D. Awschalom, and M. L. Roukes, Phys. Rev. Lett. **90**, 107201 (2003).
[10] L. Berger and B. Bergmann, in *The Hall Effect and Its Applications*, edited by C. L. Chien and C. R. Westgate (Plenum, New York, 1980), pp. 43–76.
[11] K. W. Edmonds, R. P. Campion, K. Y. Wang, A. C. Neumann, B. L. Gallagher, C. T. Foxon, and P. C. Main, J. Appl. Phys. **93**, 6787 (2003).
[12] T. Jungwirth, Q. Niu, and A. H. MacDonald, Phys. Rev. Lett. **88**, 207208 (2002).
[13] M. Abolfath, T. Jungwirth, J. Brum, and A. H. MacDonald, Phys. Rev. B **63**, 054418 (2001).
[14] T. Dietl, H. Ohno, and F. Matsukura, Phys. Rev. B **63**, 195205 (2001).
[15] G. A. Prinz, Science **282**, 1660 (1998).
[16] I. Zutic, J. Fabian, and S. Das Sarma, Rev. Mod. Phys. **76**, 323 (2004).
[17] S. J. Pearton, D. P. Norton, R. Frazier, S. Y. Han, C. R. Abernathy, and J. M. Zavada, IEE Proc.: Circuits Devices Syst. **152**, 312 (2005).
[18] T. Jungwirth, M. Abolfath, J. Sinova, J. Kučera, and A. H. MacDonald, Appl. Phys. Lett. **81**, 4029 (2002).
[19] X. Liu and J. K. Furdyna, J. Phys.: Condens. Matter **18**, R245 (2006).
[20] M. Sawicki, F. Matsukura, A. Idziaszek, T. Dietl, G. M. Schott, C. Ruester, C. Gould, G. Karczewski, G. Schmidt, and L. W. Molenkamp, Phys. Rev. B **70**, 245325 (2004).
[21] M. Sawicki, K.-Y. Wang, K. W. Edmonds, R. P. Campion, C. R. Staddon, N. R. S. Farley, C. T. Foxon, E. Papis, E. Kamińska, A. Piotrowska, T. Dietl, and B. L. Gallagher, Phys. Rev. B **71**, 121302(R) (2005).
[22] K. Hamaya, T. Taniyama, Y. Kitamoto, R. Moriya, and H. Munekata, J. Appl. Phys. **94**, 7657 (2003).
[23] K. Hamaya, T. Watanabe, T. Taniyama, A. Oiwa, Y. Kitamoto, and Y. Yamazaki, Phys. Rev. B **74**, 045201 (2006).
[24] J. Daeubler, S. Schwaiger, M. Glunk, M. Tabor, W. Schoch, R. Sauer, and W. Limmer, Physica E (Amsterdam) **40**, 1876 (2008).
[25] W. Limmer, M. Glunk, J. Daeubler, T. Hummel, W. Schoch, R. Sauer, C. Bihler, H. Huebl, M. S. Brandt, and S. T. B. Goennenwein, Phys. Rev. B **74**, 205205 (2006).
[26] S. T. B. Goennenwein, T. Graf, T. Wassner, M. S. Brandt, M. Stutzmann, J. B. Philipp, R. Gross, M. Krieger, K. Zürn, P. Ziemann, A. Koeder, S. Frank, W. Schoch, and A. Waag, Appl. Phys. Lett. **82**, 730 (2003).
[27] J. C. Harmand, T. Matsuno, and K. Inoue, Jpn. J. Appl. Phys., Part 2 **28**, L1101 (1989).
[28] R. R. Birss, *Symmetry and Magnetism* (North-Holland, Amsterdam, 1966).
[29] J. P. Jan, in *Solid State Physics*, edited by F. Seitz and D. Turnbull (Academic, New York, 1957), Vol. 5, pp. 1–96.
[30] T. McGuire and R. Potter, IEEE Trans. Magn. **11**, 1018 (1975).
[31] R. R. Birss, Proc. Phys. Soc. London **75**, 8 (1960).
[32] A. W. Rushforth, K. Výborný, C. S. King, K. W. Edmonds, R. P. Campion, C. T. Foxon, J. Wunderlich, A. C. Irvine, P. Vašek, V. Novák, K. Olejník, J. Sinova, T. Jungwirth, and B. L. Gallagher, Phys. Rev. Lett. **99**, 147207 (2007); A. W. Rushforth, K. Výborný, C. S. King, K. W. Edmonds, R. P. Campion, C. T. Foxon, J. Wunderlich, A. C. Irvine, P. Vašek, V. Novák, K. Olejník, A. A. Kovalev, J. Sinova, T. Jungwirth, and B. L. Gallagher, JMMM for Conference Proceedings of WUN-SPIN, New York, UK, 2007 (unpublished); arXiv:0712.2581 (unpublished).
[33] W. Döring, Ann. Phys. **32**, 259 (1938).
[34] S. T. B. Goennenwein, M. Althammer, C. Bihler, A. Brandlmaier, S. Geprägs, M. Opel, W. Schoch, W. Limmer, R. Gross, and M. S. Brandt, Phys. Status Solidi (RRL) **2**, 96 (2008).
[35] A. W. Rushforth, E. De Ranieri, J. Zemen, J. Wunderlich, K. W. Edmonds, C. S. King, E. Ahmad, R. P. Campion, C. T. Foxon, B. L. Gallagher, K. Výborný, J. Kučera, and T. Jungwirth, arXiv:0801.0886 (unpublished).
[36] U. Welp, V. K. Vlasko-Vlasov, A. Menzel, H. D. You, X. Liu, J. K. Furdyna, and T. Wojtowicz, Appl. Phys. Lett. **85**, 260 (2004).
[37] U. Welp, V. K. Vlasko-Vlasov, X. Liu, J. K. Furdyna, and T. Wojtowicz, Phys. Rev. Lett. **90**, 167206 (2003).
[38] A. Pross, S. Bending, K. Edmonds, R. P. Campion, C. T. Foxon, and B. L. Gallagher, J. Appl. Phys. **95**, 3225 (2004).
[39] L. Thevenard, L. Largeau, O. Mauguin, G. Patriarche, A. Lemaître, N. Vernier, and J. Ferré, Phys. Rev. B **73**, 195331 (2006).
[40] A. Sugawara, T. Akashi, P. D. Brown, R. P. Campion, T. Yoshida, B. L. Gallagher, and A. Tonomura, Phys. Rev. B **75**, 241306(R) (2007).
[41] A. Dourlat, V. Jeudy, C. Testelin, F. Bernardot, K. Khazen, C. Gourdon, L. Thevenard, L. Largeau, O. Mauguin, and A. Lemaître, J. Appl. Phys. **102**, 023913 (2007).